Contribution from the Inorganic Chemistry Laboratory, Oxford University, Oxford OX1 3QR, England, School of Chemistry and Molecular Sciences, University of Sussex, Brighton BN1 9QJ, England, and Institut Laue Langevin, Grenoble 38042, France

Magnetic Order and Crystal Chemistry of $Nd_{2-x}Ce_xCuO_{4-\delta}$

Matthew J. Rosseinsky,*,†,‡ Kosmas Prassides,*,§ and Peter Day∥

Received November 20, 1990

Structural, magnetic, and transport properties of the $Nd_{2-x}Ce_xCuO_{4-\delta}$ ($0 \le x \le 0.15$) series are presented and contrasted with the corresponding properties of the $La_{2-x}Sr_xCuO_{4-\delta}$ series. High-intensity powder neutron diffraction shows that the long-range antiferromagnetic order of the Cu sublattice persists to higher dopant levels in the $Nd_{2-x}Ce_xCuO_{4-\delta}$ system compared to the effect of hole doping in the $La_{2-x}Sr_xCuO_{4-\delta}$ phases. This is consistent with different physical mechanisms operating, namely percolation upon electron doping due to the nonmagnetic Cu^I states versus frustration upon hole doping due to O^- or Cu^{III} states. The magnetic structure at 1.5 K remains the same for all the compositions studied, with the moment at the copper site reaching zero in the superconducting material. A representation analysis reveals the novel feature of substantial coupling between the lanthanide and the copper sublattices. This is manifested in the direction adopted by the Nd^{3+} moment (parallel to the CuO_2 basal plane), the high Néel temperature for Nd^{3+} order (ca. 2 K), and the polarization-induced moment above T_N^{Nd} that is apparent in the magnetic Bragg scattering. The importance of the Nd, Cu interaction along the *c* axis in coupling the two sublattices at the experimentally observed propagation vector ($^1/_2$, $^1/_2$, 0) is further demonstrated by using a simple isotropic exchange model. Finally, the assumption that the antiferromagnetic instability must be destroyed before the carriers become delocalized leads to an estimate for the transfer integral for the motion of the electrons in the upper Hubbard subband of 0.8 eV. It also appears possible that the reported occurrence of phase separation at high Ce dopant levels may be related to both the destruction of the Néel state and the delocalization of the electrons, close to the onset of superconductivity.

Introduction

One of the most interesting areas of cuprate chemistry has been the discovery of high-temperature superconductivity in formally reduced Cu^{II} oxides, i.e. "electron-doped" n-type materials[1] containing Cu^I. This has served to focus theoretical attention on models which are symmetric to electron and hole doping of the $Cu^{II}O_2^{2-}$ layers that form the unifying structural feature of the cuprate perovskites by drawing a chemical and physical contrast with the p-type oxidized cuprates ($La_{2-x}Sr_xCuO_{4-\delta}$, $YBa_2Cu_3O_{7-\delta}$, $Bi_2(Sr_{2-x}Ca_x)CuO_6$). The initial n-doped materials were found in the $Nd_{2-x}Ce_xCuO_{4-\delta}$ series with $T_{c,max}^{onset} = 27$ K, $T_c^{Meissner} = 20$ K, and up to 60% Meissner fractions, with electron doping suggested both by Ce^{IV} formation and negative thermopower and Hall effect. This was followed by elegant synthetic work producing the first successful fluorination[2] of a high-T_c cuprate to give $Nd_2CuO_{3.82}F_{0.18}$ with $T_c = 23$ K. Apart from the contrast with all other cuprate superconductors in the nature of the charge carriers, another aspect of the evolution of the electronic properties with doping of great interest is the much *narrower* range of dopant concentration over which superconducting behavior is found ($0.14 \le x_{sc} \le 0.18$).[1,3-5]

Our initial work on this system involved refinement of high-resolution powder neutron diffraction profiles[6] of $Nd_{2-x}Ce_xCuO_{4-\delta}$ ($x = 0$, 0.01, 0.05) and the first solution of the magnetic structure[7,8] of $Nd_{2-x}Ce_xCuO_{4-\delta}$ ($x = 0$, 0.03; $\delta = 0$, 0.06) at 1.5 K with fascinating preliminary conclusions, together with a more wide-ranging study of the influence of the Cu oxidation state on the competition between the K_2NiF_4 (O,T) and T′ structure types in the $La_{2-x-y}Pr_xSr_yCuO_{4-\delta}$ system.[6,9] Recently, a very careful neutron diffraction study[10,11] provided evidence for phase separation in the $Nd_{2-x}Ce_xCuO_{4-\delta}$ system, in much the same way as in $La_2CuO_{4+\delta}$, where phase separation results from segregation of interstitial oxygen defects.[12] However, using very high resolution powder neutron diffraction, we have recently shown[13] that the lower bound on the largest value of *x* for which a single phase may be prepared in this system is 0.07. Here we report a more extensive investigation of the magnetic and structural properties of the $Nd_{2-x}Ce_xCuO_{4-\delta}$ phase diagram by powder neutron diffraction and discuss the consequences of our results for the transport properties of this system.

Experimental Section

$Nd_{2-x}Ce_xCuO_{4-\delta}$ compounds ($x = 0.01$, 0.03, 0.05, 0.07, 0.15) were prepared by multistep solid-state reactions and $Nd_2CuO_{4-\delta}$ by a citrate sol-gel route, as described before.[6,13] Phase purity was confirmed by powder X-ray diffraction. Energy dispersive X-ray fluorescence analysis performed on 10 crystallites of the $x = 0.15$ sample on a JEOL 2000 FX TEMSCEM microscope indicated excellent homogeneity of the Ce distribution ($\Delta x/x = 0.06$) and gave a value for the Nd/Cu ratio of 1.87 (4), using a Nd_2CuO_4 sample as a standard. The oxygen concentrations were measured by thermogravimetric reduction of 100-mg samples (weighed to 10 ppm) in platinum crucibles in a 5% H_2-95% Ar atmosphere on a Stanton Redcroft STA785 thermobalance. A maximum temperature of 700 °C was chosen to avoid reduction of CeO_2 to $CeO_{2-\delta}$.[14] Table I (supplementary material) shows the absolute and percentage weight losses observed and the deduced compositions. Four-probe ac conductivity measurements at a frequency of 15 Hz were performed on pellets of typical dimensions $3 \times 1 \times 1$ mm^3 between 4.2 and 300 K in an Oxford Instruments CF204 cryostat.

High-resolution powder neutron diffraction data were collected at the High Resolution Powder Diffractometer (HRPD) on the ISIS spallation neutron source at the Rutherford Appleton Laboratory; data collection on the $x = 0.07$ sample has been described elsewhere.[13] The $x = 0.15$ data were recorded between 30 000 and 120 000 μs (angular range of detectors 160-176°), normalized to the incident beam profile[15] and refined by using the TF12LS code, incorporating a Voigt function peaks-shape description and fitting the background to a 5th order Chebyshev

* To whom correspondence should be addressed.
† Oxford University.
‡ Current address: AT&T Bell Laboratories, Murray Hill, NJ 07974.
§ Sussex University.
∥ Institut Laue Langevin.

(1) Tokura, Y.; Takagi, H.; Uchida, S. *Nature* **1989**, *337*, 345.
(2) James, A. C. W. P.; Zahurak, S. M.; Murphy, D. W. *Nature* **1989**, *338*, 240.
(3) Tarascon, J.-M.; Wang, E.; Greene, L. H.; Bagley, B. G.; Hull, G. W.; D'Egidio, S. M.; Miceli, P. F.; Wang, Z. Z.; Jing, T. W.; Clayhold, J.; Brawner, D.; Ong, N. P. *Phys. Rev. B* **1989**, *40*, 4494.
(4) Hirochi, K.; Hayashi, S.; Adachi, H.; Mitsuyu, T.; Himo, T.; Setsune, K.; Wasa, K. *Physica C* **1989**, *160*, 273.
(5) Liang, G.; Chen, J.; Croft, M.; Ramanujachary, K. V.; Greenblatt, M.; Hedge, M. *Phys. Rev. B* **1989**, *40*, 2646.
(6) Rosseinsky, M. J.; Prassides, K.; Day, P. *Physica C* **1989**, *161*, 21.
(7) Rosseinsky, M. J.; Prassides, K.; Day, P. *J. Chem. Soc., Chem. Commun.* **1989**, 1734.
(8) Rosseinsky, M. J.; Prassides, K. *Physica C* **1989**, *162-164*, 522.
(9) Rosseinsky, M. J.; Prassides, K. *Physica B* **1990**, *165*, 1187.
(10) Lightfoot, P.; Richards, D. R.; Dabrowski, B.; Hinks, D. G.; Pei, S.; Marx, D. T.; Mitchell, A. W.; Zheng, Y.; Jorgensen, J. D. *Physica C* **1990**, *168*, 627.
(11) Jorgensen, J. D.; Hinks, D. G.; Lightfoot, P.; Richards, D. R.; Dabrowski, B.; Pei, S.; Marx, D. T.; Mitchell, A. W.; Zheng, Y. *Physica B* **1990**, *165*, *166*, 1509.
(12) Jorgensen, J. D.; Dabrowski, B.; Pei, S.; Hinks, D. G.; Soderholm, L.; Morosin, B.; Schirber, J. E.; Venturini, E. L.; Ginley, D. S. *Phys. Rev. B* **1988**, *38*, 11337.
(13) Rosseinsky, M. J.; Prassides, K. *Europhys. Lett.* **1991**, *14*, 551.
(14) Oh-ishi, K.; Kikuchi, M.; Syono, Y.; Kobayashi, N.; Muto, Y. *J. Solid State Chem.* **1989**, *83*, 237.
(15) Barnes, A. C.; David, W. I. F.; Ibberson, R. M. Personal communication.

0020-1669/91/1330-2680$02.50/0

Table III. Selected Bond Distances, Unit Cell Volumes, and c/a Ratios in $Nd_{2-x}Ce_xCuO_{4-\delta}$

T/K	compd	V/Å^3	c/a	Cu–O(1)/Å	Ln–O(1)/Å	Ln–O(2)/Å
4.2	Nd_2CuO_4	188.234 (5)	3.0848 (1)	1.9685	2.3213 (5)	2.6713 (6)
4.2	$Nd_{1.99}Ce_{0.01}CuO_{3.93}$	188.214 (5)	3.0834 (1)	1.9687	2.3218 (5)	2.6704 (7)
4.2	$Nd_{1.95}Ce_{0.05}CuO_{3.95}$	188.105 (5)	3.0819 (1)	1.9686	2.3217 (5)	2.6693 (4)
300	$Nd_{1.93}Ce_{0.07}CuO_{3.96}$	187.757 (2)	3.0733 (2)	1.9693	2.3213 (1)	2.6612 (1)
4.2	$Nd_{1.85}Ce_{0.15}CuO_{3.98}$	186.975 (2)	3.0599 (3)	1.9694	2.3214 (1)	2.6573 (1)

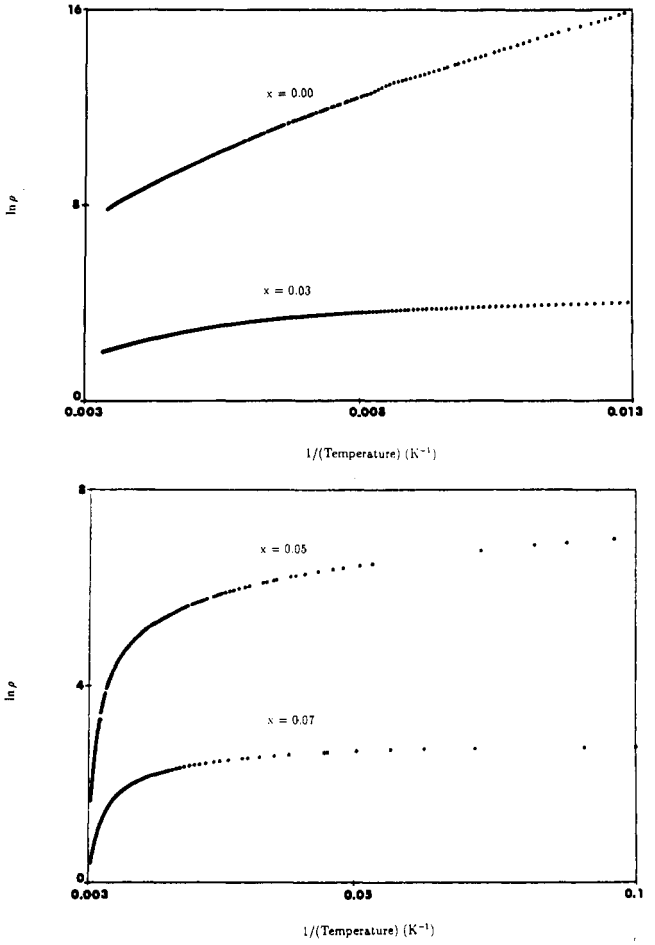

Figure 1. Arrhenius plots of the resistivity of $Nd_{2-x}Ce_xCuO_{4-\delta}$: (a, top) x = 0.0, 0.03; (b, bottom) x = 0.05, 0.07.

polynomial.[16] An absorption correction of the form $(a + b\lambda)$ was applied. Neutron diffraction patterns to investigate magnetic order of the $S = {}^1/_2$ Cu^{2+} ions when the expected intensity is very weak were collected on the high-intensity multidetector diffractometer D1B at the Institut Laue Langevin over the temperature range 1.5–300 K with a mean wavelength λ = 2.52 Å over an angular 2θ range 10–90°. Typical collection times were 3–4 h for the materials in which only Cu^{2+} moments were ordered; 30 min was sufficient if rare-earth ordering was observed.

Results and Data Analysis. X-ray diffraction and analytical electron microscopy confirmed the phase purity and homogeneity of the samples. Figure 1 displays the temperature dependence of the resistivity of the $Nd_{2-x}Ce_xCuO_{4-\delta}$ materials; the x = 0.15 compound displays superconductivity with T_c^{onset} = 24 K and T^0_c = 19 K and a negative thermal coefficient of resistivity above T_c, while both the magnitude and temperature dependence of the resistivities of the other samples decrease with increasing dopant level x. In contrast to those of the $La_{2-x}Sr_xCuO_{4-\delta}$ materials, the transport properties of the ceramic samples are different from those of single crystals; for example, superconducting single crystals of $Nd_{1.85}Ce_{0.15}CuO_4$ show metallic temperature dependence of the resistivity[17] above T_c. The equation $\rho = \rho_0(T/T_0)^{1/2}\exp[-(T_0/T)^{1/d+1}]$ describing d-dimensional variable-range hopping did not fit the temperature-dependent conductivity for any of the $Nd_{2-x}Ce_xCuO_{4-\delta}$ materials, in contrast to the hole-doped series $La_{2-x}Sr_xCuO_{4-\delta}$.[6,18-20]

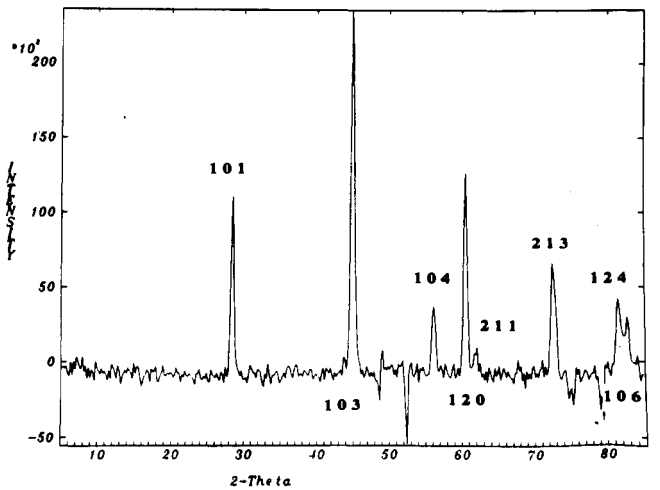

Figure 2. Difference plot of the diffraction profiles of Nd_2CuO_4 at 1.5 and 50 K (λ = 2.52 Å).

Structure Refinements. The structure refinements of the diffraction profiles of the x = 0, 0.01, 0.05, and 0.07 samples have been presented elsewhere.[6,13] Further attempts to refine the data by using orthorhombic subgroups of the tetragonal space group $I4/mmm$ ($Immm$ with basal plane dimensions $a_O \sim b_O \sim a_T$ and $Fmmm$ with $a_O \sim b_O \sim 2^{1/2}a_T$) were unstable as the a_O and b_O axes interchanged between refinement cycles and did not differ from each other by more than one standard deviation. Also refinement of the O-site occupanices on the axial and equatorial O sites showed very small deviations from stoichiometry, not exceeding the estimated standard deviations for the x = 0 and x = 0.01 samples, whereas a significant vacancy concentration, distributed almost equally over both sites, was found for the x = 0.05 sample; in the latter case, we obtained δ = 0.07 (4) from the Rietveld refinement, while the TGA measurements yielded δ = 0.05 (2). The x = 0.07 sample is particularly interesting in view of the report[10,11] that in this series of compounds single-phase materials are formed only for the undoped compound Nd_2CuO_4 and the optimum superconducting composition $x \sim 0.165$. Phase separation occurs and was rationalized by using a simple Hückel model with no inclusion of electron correlation effects but taking into account the competition between the Madelung and the electronic energy of the system as a function of d-electron count (formal Cu oxidation state).[21] Using data of very high resolution (5 times higher than in ref 10) and allowing only for a small amount of sample broadening, we have found[13] no indication of a secondary phase in the x = 0.07 sample. Assuming that indeed phase separation may be occurring in this system, our result has set a lower bound of x = 0.07 on the largest value of x for which a single phase may be prepared.

Careful examination of selected reflections of the diffraction profile of $Nd_{1.85}Ce_{0.15}CuO_{4-\delta}$ obtained on HRPD confirmed that this sample was single phase.[10,11] The refinement of the profile converged to χ^2 = 2.70, R_{wp} = 6.30%, and R_e = 3.83% (Table II (supplementary material)). Table III shows the Cu–O and the two Ln–O bond lengths together with the c/a ratio and the cell volume in the $Nd_{2-x}Ce_xCuO_{4-\delta}$ series.

Magnetic Neutron Diffraction. We discuss now the analysis of the magnetic neutron diffraction data of $Nd_{2-x}Ce_xCuO_{4-\delta}$, starting with the analysis of the magnetic structure of Nd_2CuO_4 at 1.5 K. Subtraction of the 50 K from the 1.5 K data set reveals the presence of seven Bragg peaks (Figure 2) in the low-temperature pattern, which are absent at high

(16) David, W. I. F.; Ibberson, R. M.; Wilson, C. C. *Rutherford Appleton Laboratory Report RAL-88-103*, 1988.
(17) Tarascon, J.-M.; Wang, E.; Greene, L. H.; Bagley, B. G.; Hull, G. W.; D'Egidio, S. M.; Miceli, P. F.; Wang, Z. Z.; Jing, T. W.; Clayhold, J.; Brawner, D.; Ong, N. P. *Physica C* **1989**, *162–164*, 285.
(18) Rosseinsky, M. J.; Prassides, K.; Day, P. *J. Mater. Chem.*, in press.
(19) Kastner, M. A.; Birgeneau, R. J.; Chen, C. Y.; Ching, Y. M.; Gabbe, R. D.; Jenssen, H. P.; Junk, T.; Peters, C. J.; Picone, P. J.; Thio, T.; Thurston, T. R.; Tuller, H. L. *Phys. Rev. B* **1988**, *37*, 111.
(20) Birgeneau, R. J.; Chen, C. Y.; Gabbe, R. D.; Jenssen, H. P.; Kastner, M. A.; Peters, C. J.; Picone, P. J.; Thio, T.; Thurston, T. R.; Tuller, H. L. *Phys. Rev. Lett.* **1987**, *59*, 1329.
(21) Baird, N. C.; Burdett, J. K. *Physica C* **1990**, *168*, 637.

temperature and are assigned to the onset of magnetic order. Data were also recorded in the 1.5–6 K temperature range in small temperature steps, and at 6 K the magnetic peaks are greatly reduced in intensity. The scans at higher temperatures contained very weak scattering at the $(^1/_2, ^1/_2, 1)$ position up to approximately 200 K, but despite much longer run times, it could not be measured with good statistical precision. In view of this, subsequent analysis concentrated on the low-temperature data.

The seven Bragg peaks observed at 1.5 K (Figure 2) may be indexed on the basis of an enlarged magnetic unit cell with dimensions $2^{1/2}a \times 2^{1/2}a \times c$. In view of the possible existence of magnetic moments on both the neodymium and copper sublattices, a representation analysis of possible magnetic structures[22] was performed. The initial step involves identification of the point group of the wavevector $G(\mathbf{k})$ (i.e. the subset of those operations of $I4/mmm$ that leave $\mathbf{k}$ invariant). Here the reduced propagation vector of the magnetic structure is $\mathbf{k} = (^1/_2, ^1/_2, 0)$, which corresponds to the X point of the body-centered tetragonal Brillouin zone, and $G(\mathbf{k})$ is mmm (D_{2h}). There are three Bravais sublattices, one associated with the Cu site at (000) and two with the Nd sites at (00z) and (00$\bar{z}$). Furthermore, in the larger body-centered crystallographic cell, the effect of the body-centering translation $\tau = (^1/_2, ^1/_2, ^1/_2)$ is taken into account by a phase shift $\mathbf{S}(\mathbf{r} + \tau) = \mathbf{S}(\mathbf{r}) \exp(i\mathbf{k}\cdot\tau)$, where $\mathbf{k}$ is the propagation and $\mathbf{r}$ the position vector.

We then construct the reducible representations for the Nd^{3+} and Cu^{2+} ions using the behavior of the axial magnetic moment vectors under the crystallographic symmetry operations. The transformation matrices T are defined as $\mathbf{T} = \mathbf{R} \otimes \Delta$, where $\mathbf{R}$ is the rotation matrix associated with the symmetry operation R of $G(\mathbf{k})$ (multiplied by $\det(R)$ to take into account the axial nature of the moment vectors). The elements of Δ are given by $\Delta_{mn} = \delta_{mn} \exp(i\mathbf{k}\cdot[\mathbf{r}(m) - R\mathbf{r}(n)])$ with $\delta_{mn} = 1$, if m transforms into n under the symmetry operation R and 0 otherwise. $\mathbf{k}$ is the wavevector $(^1/_2, ^1/_2, 0)$. These matrices provide a $3r$-dimensional unitary multiplier representation of $G(\mathbf{k})$, which may be reduced in the usual manner

$$n^j(\mathbf{k}) = (1/h)\sum \chi^*[T(\mathbf{k},R)]\chi^j[(\mathbf{k},R)] \quad (1)$$

where n^j is the number of times the representation Γ_j occurs in the decomposition and h is the order of $G(\mathbf{k})$. The T matrices are then used to project out basis functions transforming as the irreducible representations, Ψ_Γ. The basis functions spanning each representation using the x, y, and z components of spins at the Cu and the Nd sites are found to be

$$\begin{array}{llllll} \Gamma_{Cu} = B_{1g} + & B_{2g} + & B_{3g} & & & \\ \Psi_\Gamma \quad m_z & m_y & m_x & & & \\ \Gamma_{Nd} = B_{1g} + & B_{2g} + & B_{3g} + & A_u + & B_{2u} + & B_{3u} \\ \Psi_\Gamma \quad m_z^I+m_z^{II} & m_y^I+m_y^{II} & m_x^I+m_x^{II} & m_z^I-m_z^{II} & m_y^I-m_y^{II} & m_x^I-m_x^{II} \end{array} \quad (2)$$

Since the spin Hamiltonian must be invariant under the symmetry operations of the system, only basis functions transforming according to the same representation are admissible to second order. The magnetic structure is then constructed as a linear combination of basis vectors belonging to the same irreducible representation. Hence, inspection of the basis functions in eq 2 shows that the spins on the Nd^{3+} and Cu^{2+} sublattices must point in the same direction and that only the in-phase combination of spins on the Nd^{3+} sublattice is compatible with the existence of moments on the Cu^{2+} sites.

Since there are several well-resolved magnetic peaks in the 1.5 K profile, we employ integrated intensity methods to solve the magnetic structure to avoid any systematic errors arising from peak-shape assumptions. The first step is to construct structure factors in the enlarged nuclear cell with the configurational (+/−) spin symmetry corresponding to $\mathbf{k} = (^1/_2, ^1/_2, 0)$. The condition $h + k = 2n + 1$ on the magnetic reflections implies C anticentering. The calculated magnetic structure factor for the (100) reflection is the largest in this configurational spin symmetry. Then the absence of (100) implies that the spin must lie parallel to the face on which the magnetic structure is centered. This inequivalence of (hkl) and (khl) classes of reflection requires alteration of Shirane's expression[23] for the magnetic interaction term $\langle q^2 \rangle$ in uniaxial systems, as, due to the centering, we can only distinguish relatively, but not absolutely, between a and b.

Initially we only assigned spins on the Nd^{3+} sites and calculated the magnetic structure factors for both the in-phase and out-of-phase combinations of the Nd^{3+} spins. The out-of-phase combination was clearly incorrect, since it failed to predict any intensity for the (120) peak. On the other hand, the in-phase combination predicts all the observed peaks but their ratios of intensities do not agree with experiment. In view then of the magnetic scattering observed at the (011) position at higher temperatures, a moment was also introduced on the Cu^{2+} sublattice along the (100) direction of the enlarged cell. Magnetic intensities A are then evaluated according to the relationship

$$A = C\gamma_0 I_M m_{hkl}/\sin\theta \sin 2\theta$$

$$I_M = \langle 1 - (\mathbf{q}\cdot\mu)^2)(F^2_{M,Nd}f^2_{Nd}(\mathbf{q}) + F_{M,Nd}F_{M,Cu}f_{Nd}(\mathbf{q})f_{Cu}(\mathbf{q}) + F^2_{M,Cu}f^2_{Cu}(\mathbf{q})) \quad (3)$$

where $\mathbf{q}$ and μ are unit vectors in the directions of scattering vector and magnetic moment, respectively, the brackets indicating an average over all equivalent reflections. C is a scale factor evaluated from the weak (002) and (202) nuclear peaks by using the positional parameters obtained from Rietveld refinements of the high-resolution neutron data to evaluate the calculated nuclear structure factors, m_{hkl} is the multiplicity of the (hkl) reflection, and $\gamma_0 = 0.54 \times 10^{-12}$ cm. F_M values are magnetic structure factors for the two sublattices, $F_M = \sum_i \mathbf{m}_i e^{i\mathbf{q}\cdot\mathbf{r}_i}$, summed over all magnetic atoms, $\mathbf{m}_i$ values are the magnetic interaction terms, and $f(\mathbf{q})$ values are the form factors. The form factor for Cu was obtained by interpolation from the measurements of Freltoft et al.[24] on La_2CuO_4. The free ion $4f^3$ Nd^{3+} form factor was calculated in the dipole approximation from the relativistic calculations of Freeman and Desclaux.[25] The model moments for an A-centered structure with Nd and Cu spins parallel to $\mathbf{a} = (100)$ were then refined.[26] The results of the refinements at 1.5 K

Table IV. Magnetic Structure Refinements for $Nd_{2-x}Ce_xCuO_{4-\delta}$ at 1.5 K

	Nd_2CuO_4[a]			$Nd_{1.97}Ce_{0.03}CuO_4$[a]		
hkl	I_{obs}	ΔI_{obs}	I_{calc}	I_{obs}	ΔI_{obs}	I_{calc}
011	2.65	0.10	2.65	1.97	0.20	1.97
013	22.30	0.50	22.25	17.6	1.8	16.6
120	17.40	0.60	17.52	12.0	1.2	13.1
213	7.26	0.70	7.15	5.4	1.0	6.3
m_{Cu}/μ_B		0.507 (3)			0.45 (4)	
m_{Nd}/μ_B		1.136 (2)			0.98 (2)	
R^I_{mag}/%		0.6			7.9	
χ^2		1.04			1.02	

	$Nd_{1.95}Ce_{0.05}CuO_4$			$Nd_{1.93}Ce_{0.07}CuO_4$		
hkl	I_{obs}	ΔI_{obs}	I_{calc}	I_{obs}	ΔI_{obs}	I_{calc}
011	2.55	0.16	2.575	1.90	0.06	1.90
013	18.96	0.46	18.72	12.78	0.08	12.78
104				2.69	0.04	2.78
120	14.76	0.80	14.00	9.97	0.08	10.04
213	4.69	0.42	4.01	4.60	0.30	4.21
m_{Cu}/μ_B		0.43 (4)			0.336 (4)	
m_{Nd}/μ_B		1.06 (5)			0.886 (2)	
R^I_{mag}/%		7.0			2.3	
χ^2		1.90			1.50	

	$Nd_{1.85}Ce_{0.15}CuO_4$		
hkl	I_{obs}	ΔI_{obs}	I_{calc}
011	0.54	0.03	0.47
013	0.99	0.06	1.05
120	0.82	0.04	0.83
213	0.27	0.03	0.34
m_{Cu}/μ_B[b]		0.00[b]	
m_{Nd}/μ_B		0.60 (2)	
R^I_{mag}/%[c]		8.0	
χ^2[d]		2.98	

[a] Reference 7. [b] Not varied in final refinement. [c] $R^I_{mag} = 100\sum_k (I_M^{obs,k} - I_M^{cal,k})/I_M^{obs,k}$. [d] $\chi^2 = 1/(n_{obs} - n_{par})\sum_k [(I_M^{obs,k} - I_m^{cal,k})/\Delta I_M^{obs,k}]^2$.

(22) Bertaut, E. F. *Acta Crystallogr.* **1968**, *A24*, 217.
(23) Shirane, G. *Acta Crystallogr.* **1959**, *2*, 282.
(24) Freltoft, T.; Shirane, G.; Mitsuda, S.; Remeika, J. P.; Cooper, A. S. *Phys. Rev. B* **1988**, *37*, 137.
(25) Freeman, A. J.; Desclaux, J. P. *J. Magn. Magn. Mater.* **1979**, *12*, 4.
(26) The refinement was performed by using the nonlinear least-squares NAG routine E04GEF, while estimated standard deviations were calculated from the diagonal elements of the variance–covariance matrix by using the NAG routine E04YCF. Note that the estimated standard deviations reflect the statistical precision rather than the absolute accuracy of the measurements, which are limited by the nuclear scale factors.

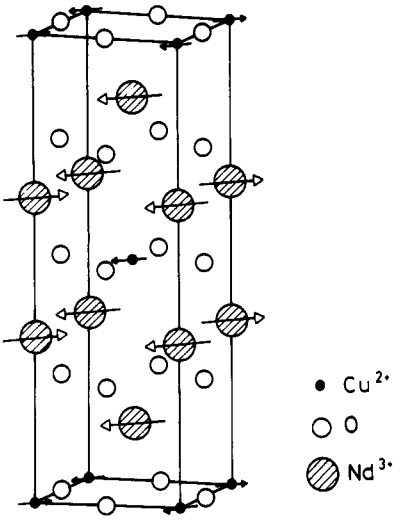

Figure 3. Magnetic structure of $Nd_{2-x}Ce_xCuO_{4-\delta}$ at 1.5 K.

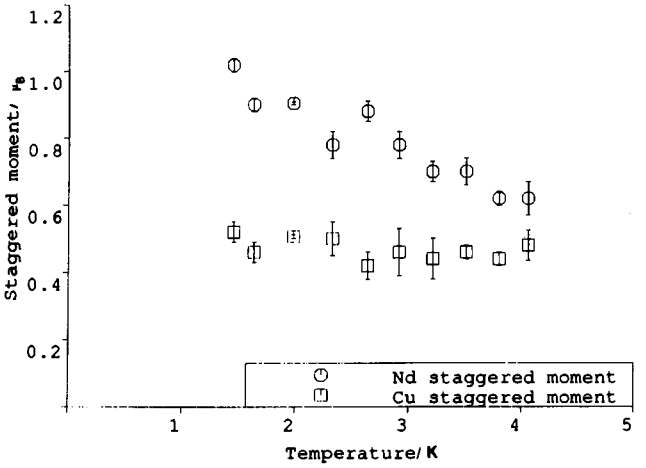

Figure 4. Temperature evolution of the Nd and Cu staggered moments for $Nd_{1.97}Ce_{0.03}CuO_{4-\delta}$.

are given in Table IV. An extra reflection, (104), was included in the $x = 0.07$ refinement to test the validity of the model; it was obtained by subtraction of the 250 K data (unambiguously higher than T_N) from the 1.5 K data set. These results clearly show the 1.5 K magnetic structure is well defined by the model presented in Figure 3. However, the fit to the $Nd_{1.85}Ce_{0.15}CuO_4$ data is significantly poorer and may indicate that the model is no longer valid, though all attempts to introduce additional components of the Nd spin or use of out-of-phase structure were unsuccessful. In this superconducting phase, the moment at the copper site is zero.

The magnetic space group is $F_Amm'm'$, i.e. the spins lie perpendicular to the unprimed σ_{yz} mirror phase (defined in the $2^{1/2}a \times 2^{1/2}a \times c$ cell). High-resolution powder neutron diffraction reveals the T′ phases remain tetragonal[6,9,13] to 1.5 K; the magnetic structure deduced here has orthorhombic symmetry, and as has been pointed out,[7,27,28] noncollinear spin structures with tetragonal configurational symmetry (coherent superpositions of the $F_Amm'm'$ structure with spins rotated through 90° to give magnetic space group $P4_2/nc'm'$[27]) are indistinguishable from the present arrangement without a one-domain single crystal (cf. ref 29).

Refinements of data sets collected in small temperature steps up to 6 K on the $x = 0$ and 0.03 systems show the staggered moment at the Nd site decreasing with temperature, while the Cu moment remains constant. This implies long-range order of the Cu spins above 6 K (Figure 4). Furthermore, careful examination of the (011) region of the pattern does not reveal any magnetic intensity above 170 K, but the scans were insufficiently long to extract a reliable T_N. On the other hand, long

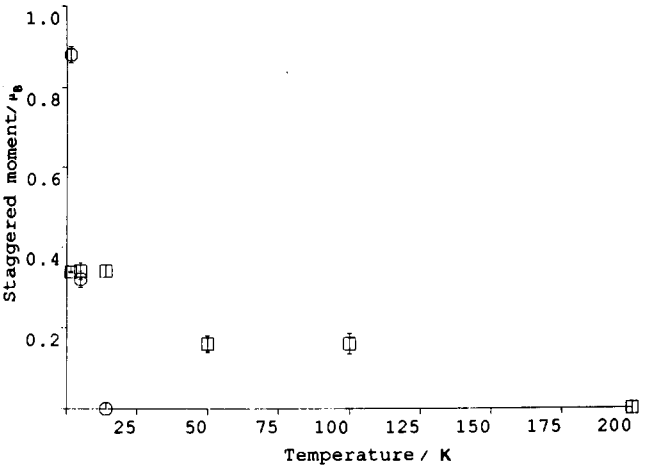

Figure 5. Temperature evolution of the Cu and Nd staggered moments for $Nd_{1.93}Ce_{0.07}CuO_{4-\delta}$.

counting times were employed to study $Nd_{1.93}Ce_{0.07}CuO_{4-\delta}$ at 50, 100, and 200 K; the variation of the Cu staggered moment is shown in Figure 5, and the Néel temperature lies between 100 and 200 K.

Discussion

Crystal Chemistry. The crystal chemistry of the "electron-doped" $Nd_{2-x}Ce_xCuO_{4-\delta}$ series presents a marked contrast to that of the "hole-doped" $La_{2-x}Sr_xCuO_{4-\delta}$ materials. The most striking difference, the adoption of different crystal structure types, may be rationalized by the smaller Nd^{3+} ion preferring the eight-coordinate cubic site in the fluorite type $Nd_2O_2^{2+}$ layers in the T′ structure to the nine-coordinate site in the rock-salt $La_2O_2^{2+}$ layers in the K_2NiF_4 structure. Second, the T′ materials do not undergo the orthorhombic distortion characterized by the octahedral tilting motion found in $La_{2-x}Sr_xCuO_{4-\delta}$. In the same way the tilting of the CuO_6 groups in the hole-doped system may be rationalized in terms of the perovskite tolerance factor,[18,30] the crystal chemistry of the T′ phase may be discussed in terms of a tolerance factor defined by matching the Cu–O(1) to the Ln–O(1) bond length, which by simple geometry gives an expression analogous to that defined for perovskites, $t_{T'} = r_{Ln-O(1)}/2^{1/2}r_{Cu-O(1)}$. For example, $t_{T'} = 0.96$ for Nd_2CuO_4 at 5 K. This perfect bond length matching explains the absence of low-temperature tilting transitions in the T′-phase materials.[6] Table III clearly shows the interdependence of the two crucial bond lengths. The absence of the axial oxygen may also be critical. The key role of the tolerance factor in the crystal chemistry of these phases is shown by a comparison between the copper–oxygen bond lengths in Nd_2CuO_4 and Pr_2CuO_4; the smaller Nd^{3+} cation (1.249 Å vs 1.266 Å) requires, for the same tolerance factor, a shorter Cu–O distance (1.9685 Å vs 1.9775 Å). Ce doping produces a competition between the smaller ionic radius of Ce^{IV} and the increased bond length required by an increase in the number of σ^* electrons as reduction to Cu(I) occurs. The decrease in the (c/a) ratio as the doping increases is also apparent from Table III and shows Ce is present as Ce^{IV} rather than Ce^{III} (Ce^{III} is larger and Ce^{IV} smaller than Nd^{3+}).[31] This is also reflected in the reduced unit cell volumes, also shown in Table III.

In comparison with the equatorial copper–oxygen bond lengths of ~1.9 Å or less in the K_2NiF_4 phases, the equatorial bond lengths in the T′ phases are much longer, an aspect of the crystal chemistry of the two classes of material that may be important in determining how they can be doped.[31] The long equatorial bond lengths put the planes under tension, which allows further lengthening by electron doping. By contrast, the K_2NiF_4 phases feature short Cu–O bonds, which put the layers under compression and allow further hole doping to compress the $[CuO_2]^{2-}$ layers. The tolerance factors for the two structures therefore control the

(27) Cox, D. E.; Goldman, A. I.; Subramanian, M. A.; Gopalakrishnan, J.; Sleight, A. W. *Phys. Rev. B* **1989**, *40*, 6998.
(28) Yamada, K.; Kakurai, K.; Endoh, Y. *Physica C* **1990**, *165*, 131.
(29) Skanthakumar, S.; Zhang, H.; Clinton, T. W.; Li, W.-H.; Lynn, J. W.; Fisk, Z.; Cheong, S.-W. *Physica C* **1989**, *160*, 124.
(30) Singh, K. K.; Ganguly, P.; Rao, C. N. R. *J. Solid State Chem.* **1984**, *52*, 254.
(31) Goodenough, J. B. *Supercond. Sci. Technol.* **1990**, *3*, 26.

range of oxidation states that they are compatible with; i.e., the T′ structure will favor lower copper oxidation states. This may be extended to explain why successful hole and electron doping of a single parent material, leading to superconductivity, has yet to be achieved.

Magnetic Structures. We first discuss the magnetic structure of Nd_2CuO_4. Considering initially the Cu^{2+} sublattice, the magnetic structure corresponds to the propagation vector $\mathbf{k} = (^1/_2, ^1/_2, 0)$ being parallel to the spin direction $\mu = (^1/_2, ^1/_2, 0)$, as is the case in La_2NiO_4,[32] which has the K_2NiF_4 structure. This is in contrast to La_2CuO_4,[33] which has $\mathbf{k} = (^1/_2, -^1/_2, 0)$ perpendicular to $\mu = (^1/_2, ^1/_2, 0)$; i.e., the translation $\tau = (^1/_2, ^1/_2, ^1/_2)$ corresponds to a reversal in spin direction (phase factor $e^{2\pi i\mathbf{k}\cdot\tau} = -1$) in Nd_2CuO_4 but not in La_2CuO_4 ($e^{2\pi i\mathbf{k}\cdot\tau} = 1$). After our preliminary communication[7] of the magnetic structure at 1.5 K, Yamada and co-workers[34] have undertaken extensive neutron diffraction experiments on Nd_2CuO_4 single crystals. Their work confirmed the correctness of our proposed model for the magnetic structure. Furthermore, it revealed the presence of two spin reorientation transitions between room temperature and 1.5 K. Thus, the Néel temperature for Cu order is found to be ~300 K,[35] in agreement with μSR measurements;[36] the magnetic structure is identical with the one of La_2NiO_4. At $T_t^I = 120$ K, the propagation vector changes from $(^1/_2, ^1/_2, 0)$ to $(^1/_2, -^1/_2, 0)$; i.e., a La_2CuO_4-type spin structure is adopted. This is then followed by the second transition at $T_t^{II} = 75$ K back to the La_2NiO_4-type structure.

The moment of 0.507 μ_B observed at the Cu site for Nd_2CuO_4 is markedly reduced from the value of 1.14 μ_B, predicted from $S = ^1/_2$ and $g = 2.28$. A reduction of $\Delta S \sim 0.18$ may be obtained by invoking zero-point spin fluctuations for a 2D insulator, as the Néel state is not the true ground state of the Heisenberg Hamiltonian.[37] This results in an expected value for the magnetic moment of 0.73 μ_B. The further reduction of ~30% must be due then to covalency. The moment is slightly larger than that observed in La_2CuO_4,[18,33] reflecting the decreased transfer integral resulting from the longer Cu–O bond lengths in the T′ structure.

The magnetic moment observed at the Nd^{3+} site is considerably smaller than the free-ion value of 3.27 μ_B for $^4I_{9/2}$ Nd^{3+}. This is presumably due to the influence of the cubic crystal field as the observed moment of 1.136 μ_B is consistent with a Kramers doublet ground state (Γ_6). The exact nature of the wavefunction at the Nd^{3+} site has been probed by inelastic neutron scattering measurements[38] of the crystal field transitions in Nd_2CuO_4, and it was found that a small splitting (0.35 meV for the ground-state doublet[39]) of the five crystal field doublets exists at 1.5 K, originating from a magnetic field parallel to $(^1/_2, ^1/_2, 0)$. Specific heat measurements[40] on Nd_2CuO_4 indicate that $T_N = 2$ K on the Nd sublattice, yet Figure 4 shows that ordered Nd^{3+} moments are observed at up to twice this temperature. To explain this, we have to invoke a superexchange J_{Nd-Cu} interaction; thus the Cu moments order at a much higher temperature than the Nd moments, since $J_{Cu-Cu} \gg J_{Nd-Nd}$; then they induce a polarized nonzero time-averaged moment along the Cu spin direction at the Nd^{3+} site, with paramagnetic fluctuating y and z components for $T >$ 2 K, which become zero and static for $T < 2$ K. This gives rise to the observed contribution to the magnetic Bragg scattering in Nd_2CuO_4 and $Nd_{1.97}Ce_{0.03}CuO_4$ at temperatures $T_N^{Cu} > T > T_N^{Nd}$. The Néel temperature of 2 K and the existence of the nonzero time-averaged component for $T > T_N$ may be contrasted with the behavior[41] of eight-coordinate cubic Nd^{3+} in $NdBa_2Cu_3O_{6.85}$, where $T_N = 0.551$ K. Here, there is no moment above T_N and the spin direction is along the c axis. The observation that the spin direction is in the ab plane in Nd_2CuO_4 shows the importance of the coupling between the Nd^{3+} and Cu^{2+} sublattices, as initially indicated by the success of the representation analysis in determining the magnetic structure. Furthermore, the superexchange interaction J_{Nd-Cu} is greater than J_{Nd-Nd} and J_{Nd-Cu} is of the order of 10 K, as it is in this temperature range that we observe participation of the Nd^{3+} ions in the long-range order. The transition reported[35,43] at even lower temperatures (<1 K) may be due to a Nd spin reorientation, as the superexchange interaction J_{Nd-Nd} becomes comparable to k_BT. By analogy with this higher temperature ordering of the Nd^{3+} moments by those of the Cu^{2+}, one may speculate that, below the Néel temperature of the Nd^{3+} moments in superconducting $Nd_{1.85}Ce_{0.15}CuO_{4-\delta}$, polarization of the Cu sublattice may produce unusual critical field behavior.

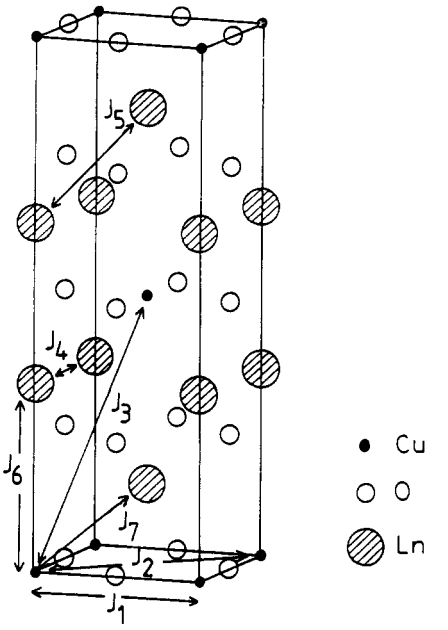

Figure 6. Exchange constants in Nd_2CuO_4.

An Isotropic Exchange Model. In general, observation of magnetic order in crystalline materials derives from the fact that the magnetic energy, consisting of an exchange, an anisotropy, and a dipolar term, is minimized for a particular ordered arrangement of magnetic moments below some transition temperature. We examine here in detail the Heisenberg isotropic exchange part of the Hamiltonian appropriate for the magnetic structure of Nd_2CuO_4, which governs high-temperature ordering, in order to establish the conditions to be satisfied by the exchange constants at the experimentally observed wavevector. In Table V (supplementary material) and Figure 6, we define all the exchange constants and lattice translations that characterize the full network of exchange pathways between copper and neodymium atoms.

We first consider the Cu sublattice in Nd_2CuO_4 with exchange constants J_1, J_2, and J_3 (Figure 6, $|J_1| > |J_2| \gg |J_3|$). Applying

(32) Aeppli, G.; Buttrey, D. J. *Phys. Rev. Lett.* **1988**, *61*, 203.
(33) Vaknin, D.; Sinha, S. K.; Moncton, D. E.; Johnston, D. C.; Newsam, J.; Safinya, C. R.; King, H. *Phys. Rev. Lett.* **1987**, *58*, 2802.
(34) Matsuda, M.; Yamada, K.; Kakurai, K.; Kadowski, H.; Thurston, T. R.; Endoh, Y.; Hidaka, Y.; Birgeneau, R. G.; Gehring, P. M.; Moudden, A. H.; Shirane, G. *Phys. Rev. B*, in press.
(35) Endoh, Y.; Matsuda, M.; Yamada, K.; Kakurai, K.; Hidaka, Y.; Shirane, G.; Birgeneau, R. J. *Phys. Rev. B* **1989**, *40*, 7023.
(36) Luke, G. M.; Sternlieb, B. J.; Uemura, Y. J.; Brewer, J. H.; Kadono, R.; Kiefl, R. F.; Kreitzman, S. R.; Riseman, T. M.; Gopalakrishnan, J.; Sleight, A. W.; Subramanian, M. A.; Uchida, S.; Takagi, H.; Tokura, Y. *Nature* **1989**, *338*, 49.
(37) de Jongh, L. J. *Solid State Commun.* **1988**, *65*, 963.
(38) Boothroyd, A. T.; Doyle, S. M.; Paul, D. McK.; Misra, D. S.; Osborn, R. *Physica C* **1990**, *165*, 17.
(39) Staub, U.; Allenspach, P.; Furrer, A.; Ott, H. R.; Cheong, S.-W.; Fisk, Z. *Solid State Commun.*, in press.
(40) Markert, J. T.; Early, E. A.; Bjornholm, T.; Ghamaty, S.; Lee, B. W.; Neumeier, J. J.; Price, R. D.; Seaman, C. L.; Maple, M. B. *Physica C* **1989**, *158*, 178.
(41) Fischer, P.; Schmid, B.; Bruesch, P.; Stucki, F.; Unternahrer, P. *Z. Phys. B* **1989**, *74*, 183.
(42) Skanthakumar, S.; Zhang, H.; Clinton, T. W.; Li, W.-H.; Lynn, J. W.; Fisk, Z.; Cheong, S.-W. *J. Appl. Phys.* **1990**, *67*, 4530.
(43) Birgeneau, R. J.; Shirane, G. *Physical Properties of High Temperature Superconductors*; Ginsberg, D. M., Ed.; World Scientific Publishing: London, 1989.

Bertaut's microscopic theory,[22] we obtain the following expression for the exchange energy of the copper Bravais sublattice:

$$E_{Cu-Cu} = 2J_1(\cos 2\pi k_x + \cos 2\pi k_y) + 4J_2 \cos 2\pi k_x \cos 2\pi k_y + 8J_3 \cos \pi k_x \cos \pi k_y \cos \pi k_z \quad (4)$$

Here k_x, k_y, and k_z are the components of the magnetic propagation vector. Both propagation vectors $\mathbf{k} = (^1/_2, ^1/_2, 0)$ (Nd_2CuO_4-type) and $\mathbf{k} = (^1/_2, -^1/_2, 0)$ (La_2CuO_4-type) satisfy the energy minimization conditions. The stability condition that the derivatives $\partial^2 E/\partial k_i \partial k_j$ must be positive definite[22] leads to the following conditions on the exchange constants for the two propagation vectors:

$$\mathbf{k} = (^1/_2, ^1/_2, 0) \qquad J_1/J_2 < 2 \qquad J_3 < 0$$
$$\mathbf{k} = (^1/_2, -^1/_2, 0) \qquad J_1/J_2 < 2 \qquad J_3 > 0 \quad (5)$$

From (4) the exchange energies for the two wavevectors are identical, $E_{Cu-Cu} = -4S^2(J_2 - J_1)$. Since $E_{Cu-Cu} < 0$, we require $J_2 > J_1$. Simple considerations from Figure 6, however, indicate that $J_2 < J_1$, and hence, J_1 is negative (antiferromagnetic) and J_2 is positive. The stability conditions in (5) show that the difference between the two propagation vectors lies in the sign of the interlayer exchange constant J_3 (ferromagnetic for the La_2CuO_4-type and antiferromagnetic for the Nd_2CuO_4-type structures). An upper limit for the Néel temperature may be obtained by $T_N \leq T_{MF} = J_2 - J_1$ by using a mean field treatment; this is, however, a large overestimate corresponding to the onset of long-range 2D correlations within the layers, the 3D order being established by the weak interlayer exchange.

The Nd–Nd interaction, on the other hand, involves two Bravais sublattices ($00z$, $00\bar{z}$) and becomes of importance at low temperatures; in the case of the superconducting compound $Nd_{1.85}Ce_{0.15}CuO_4$, it is actually the only exchange interaction present. In this case the intra- and inter-Bravais exchange interactions are given by

$$J_{11} = J_{22} = 2J_4(\cos 2\pi k_x + \cos 2\pi k_y)$$
$$J_{12} = J^*_{21} = 4J_5 \exp[2\pi i(^1/_2 - 2z)k_z] \cos \pi(k_x + k_y) \cos \pi(k_x - k_y) \quad (6)$$

with exchange constants J_4 and J_5 (Figure 6). The stability conditions then result in the following restrictions on the exchange constants:

$$J_4 > 0 \qquad J_5 < 0 \quad (7)$$

The exchange energy from eq 6 for the observed $\mathbf{k} = (^1/_2, ^1/_2, 0)$ is given by $E_{Nd-Nd} = 4S^2(J_4 + J_5)$. Using a mean field approach (more appropriate in this case where the Nd^{3+} ions form a bilayer than the case of the strictly two-dimensional sheets of Cu^{2+} ions), we obtain $T_N^{Nd} \sim 2\ K \leq T_{MF} = J_5 + J_4 \sim |J_5|$, since $|J_5| > |J_4|$.

Finally, we can discuss the coupling between the Nd^{3+} and the Cu^{2+} sublattices by introducing the exchange constants J_6 and J_7 (Figure 6). Then the exchange interaction between the Nd^{3+} and Cu^{2+} sublattices is given by

$$J_{13} = 2J_6 \cos 2\pi k_z z + 4J_7 \exp[2\pi i(z - ^1/_2)] [\cos \pi(k_x + k_y) + \cos \pi(k_x - k_y)] \quad (8)$$

In keeping with the symmetry analysis of the earlier section, the out-of-phase combination of the Nd^{3+} spins does not interact with the Cu^{2+} sublattice and its energy is equal to that calculated for the Nd spins alone, even including the Nd–Cu coupling. On the other hand, the in-phase combination of the Nd^{3+} spins and the Cu^{2+} spins interact strongly and their energies can be obtained by a simple diagonalization of the interaction matrix as

$$E_\pm = ^1/_2(J_{11} + J_{12} + J_{33}) \pm ^1/_2[8J_{13}^2 + (J_{11} + J_{12} - J_{13})^2]^{1/2} \quad (9)$$

The corresponding eigenfunctions are

$$\Psi_+ = \cos \beta\ |+\rangle + \sin \beta\ |-\rangle$$
$$\Psi_- = \sin \beta\ |+\rangle + \cos \beta\ |-\rangle \quad (10)$$

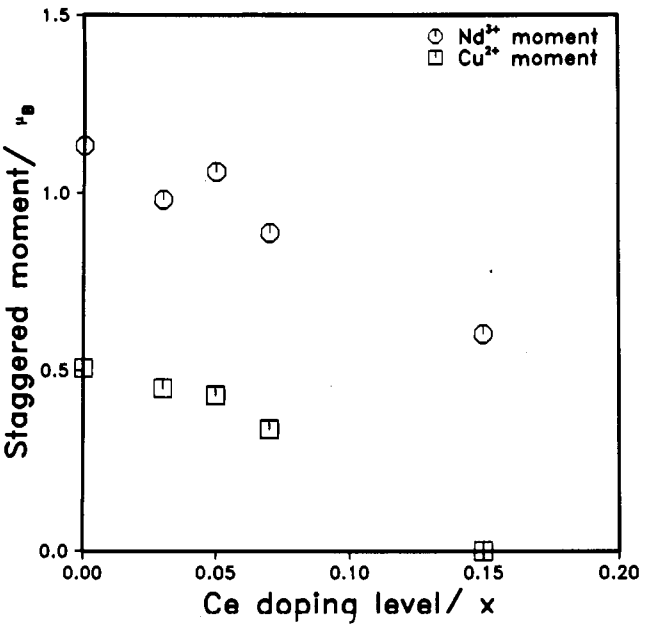

Figure 7. Variation of the Nd and Cu staggered moments as a function of Ce dopant concentration in $Nd_{2-x}Ce_xCuO_{4-\delta}$ at 1.5 K.

where $\beta = ^1/_2 \tan^{-1}[(J_{11} + J_{12} - J_{33})/8^{1/2}J_{13}]$ and $|+\rangle$ and $|-\rangle$ are the symmetric and antisymmetric combinations of the two B_{1g} modes. Substituting the values of $J_{11} \sim J_{12} \sim 2$ K, $J_{13} \sim 10$ K, and $J_{33} \sim 1000$ K in eq 10, we obtain for the ground-state wavefunction $\Psi_+ \sim 0.72|+\rangle + 0.70|-\rangle$, indicating strong mixing of the two components. This is puzzling in view of the exclusive observation of the symmetric combination of the B_{1g} modes by experiment.

It is interesting that the Nd^{3+}–Cu^{2+} coupling, expected to be the strongest (J_7 at a separation of 3.32 Å), does not contribute to the exchange interaction between the sublattices for the observed wavevector $\mathbf{k} = (^1/_2, ^1/_2, 0)$. Equation 8 shows that the interactions with alternately directed Cu spins cancel, and it is the direct Nd^{3+}–Cu^{2+} interaction along the c axis (J_6 at a separation of 4.26 Å) that provides the coupling. The observed ferromagnetic coupling may be rationalized as hopping of the Cu^{2+} spin to a vacant f orbital on the Nd^{3+} ion, where the interaction with the three neodymium spins gives a ferromagnetic interaction of order $J \sim t^2_{NdCu}K_{Nd}/U^2_{Nd}$, with K_{Nd} the intraatomic exchange energy of Nd^{3+}.

Finally, we have shown that the two magnetic structures, corresponding to the magnetic propagation vectors $(^1/_2, ^1/_2, 0)$ and $(^1/_2, -^1/_2, 0)$, have identical isotropic exchange energies as well as identical coupling to the Nd^{3+} sublattice; this demonstrates that the two phase transitions[34] observed in Nd_2CuO_4 are not driven by isotropic exchange. The dipolar energy is different in the two spin structures, but whether this can drive transitions in the region of 100 K is debatable.

Magnetic and Transport Properties of $Nd_{2-x}Ce_xCuO_{4-\delta}$. We now discuss the influence of electron doping on the magnetism and the conclusions that can be drawn about the metal–insulator transition; we particularly refer to the contrast in the transport properties of the electron- and hole-doped materials, i.e. the higher doping level required to achieve superconductivity in the T′ phases and the much narrower range over which it persists ($0.14 \leq x \leq 0.17$). The refined saturation staggered moments on the Nd and Cu sublattices decrease with increasing Ce dopant concentration, as shown in Figure 7, with no moment on the Cu sublattice at the superconducting composition. Clearly the decrease in moment with carrier concentration is much less marked in the electron-doped materials when compared with the precipitous decrease in Cu staggered moment in the hole-doped materials.[17,18,41] Also, our Cu sublattice magnetization measurements for $Nd_{1.93}Ce_{0.07}CuO_{3.96}$ show that the Néel temperature for Cu magnetic order lies between 100 and 200 K, while μSR[34] data show that the $x = 0.10$ compound has $T_N^{onset} = 240$ K with spin freezing

Table VI. Effective Delocalization of Electron Carriers over Cu Sites in $Nd_{2-x}Ce_xCuO_{4-\delta}$

Ce concn/%	reduction in moment/%	size of carrier (no. of Cu sites)
3	11	3–4
5	15	3
7	33	4–5
15	100	7/band

in the entire sample at 150 K; both experiments indicate that T_N too falls much less rapidly than in the hole-doped case.

The rapid decrease in T_N, ordered moment, and antiferromagnetic correlation length in the CuO_2 layers has been attributed[43,44] to frustration of the antiferromagnetic Cu–Cu superexchange by $2p\sigma$ holds in oxygen, producing very strong ferromagnetic near-neighbor Cu–Cu coupling, which rapidly reduces T_N. Similar frustration can be induced if next-nearest-neighbor hops are considered by the presence of Cu(III) d^8 states with a vacant $d_{x^2-y^2}$ level.[7,8,18] By virtue of the double-exchange interaction mobile Cu(III) holes will also favor ferromagnetic Cu–Cu bonds. The radically different behavior of the moment and Néel temperature on electron doping (Figure 7) suggests a different physical mechanism, namely that the localized nonmagnetic Cu^I states introduced on electron doping before the metal–insulator transition will only affect the onset of magnetic order at the percolation threshold. The metal–insulator transition seems to occur at a value of Ce^{IV} doping level very close to the onset of superconductivity, implying that the loss of antiferromagnetic order must be associated with the delocalization of the carriers. The kinetic energy of the electron carriers is minimized by allowing band motion from site to site in the Cu(II) background, which causes a loss of exchange energy as a "wrong" spin is left behind by the carrier motion. The metal–insulator transition will then occur when the carrier kinetic energy, W, and background exchange energy are equal, $W_{el} = 8t_{el}[x(1-x)/2] = 4J_{dd}$. Hence, for $J_{dd} \sim 0.1$ eV[45] and $x_c \sim 0.14$, the transfer integral may be estimated as $t_{el} \sim 0.8$ eV. This is physically reasonable as it is of the same order of magnitude as the transfer integral calculated for La_2CuO_4 (0.5 eV),[46] and the Cu(I) states that are the electron carriers will have a larger radius. Thus, carrier delocalization can occur for a physically reasonable value of the bandwidth at an appropriate carrier concentration. The reduction of the Cu moment at lower values of x, before the delocalization occurs, may be used to place an upper bound on the radius of the localized states by estimating the number of Cu sites over which the carrier is delocalized from the percentage reduction in moment (Table VI).

The result from Table VI may be interpreted as an almost constant reduction at low Ce concentration due to dilution without significant enhancement of delocalization by intercarrier overlap. However, the latter is enhanced at higher carrier concentrations possibly also reinforced by spin polaron formation. Approximately 20–25% of carriers are needed to suppress fluctuating local moments at the Cu sites within the dilution formalism. Hence, in the concentration rage 14–17%, local moments will still be present and slowly fluctuating to produce a local correlation splitting that allows "correlation bags" to form over a length scale ξ_{AF}. This may be larger than ξ_{SC} and allow resonating valence bond or spin-bag[47] pairing mechanisms to operate.

In our previous discussion, we have assumed phase purity for all the compounds in the $Nd_{2-x}Ce_xCuO_{4-\delta}$ series. However, there is a lot of evidence for multiphase behavior in these systems. The introduction of O vacancies[48] by Ar annealing at 400–700 °C seems to produce two phases in the electron diffraction patterns of $Nd_2CuO_{4-x}F_x$, $Nd_{2-x}Ce_xCuO_{4-\delta}$, and $Nd_2CuO_{4+\delta}$, one of the phases displaying a $\mathbf{q} = (1/4, 1/4, 0)$ superlattice modulation of the undistorted T′ structure adopted by the other phase. This behavior was used to explain why superconducting samples were semiconducting in the normal state in contrast to the metallic behavior of non-phase-separated superconducting single crystals[3,17,49] of the same composition. Furthermore, Jorgensen and co-workers[10,11] have elegantly shown from high-resolution powder neutron diffraction that phase separation is widely present in $Nd_{2-x}Ce_xCuO_{4-\delta}$; the two phases identified are an $x = 0.165$ phase, whose fraction is sharply increased in the superconducting region, and a second phase, whose c/a ratio decreases with increasing x. This was used to explain the higher dopant levels required to achieve superconductivity in the T′ phases and the much narrower range over which it persists ($0.14 \leq x \leq 0.17$). Such arguments could also explain our observed decrease in the Cu staggered magnetic moment upon electron doping if we take it as a weighted average of the Cu magnetic moments in the two components. The solid-solution component could presumably also produce the reduction in the T_N observed both in the μSR experiments and in our neutron measurements of $Nd_{1.93}Ce_{0.07}CuO_4$.

However, we found[13] no evidence for such behavior in our $x = 0.07$ sample using very high-resolution powder neutron diffraction measurements, a result that restricts the composition range for which phase separation is encountered but does not rule out its occurrence at higher dopant levels. What is of utmost importance is the physical origin of the phase separation. It may be due to nonequilibrium conditions in the sample preparation, as suggested in refs 10, 11, and 20. However, it may also be related to the *metal–insulator transition, which occurs very close to the onset of superconductivity as x increases.* Indeed phase separation is well-known to occur close to metal–insulator transitions. Also the Cu antiferromagnetic order is destroyed before the carriers are delocalized, suggesting that the appearance of phase separation may coincide with both the destruction of the AF order and the occurrence of the metal–insulator transition. μSR measurements[36,50] (the only technique as yet not to show evidence of phase separation) on $x \sim 0.15$ samples before (nonsuperconducting) and after (superconducting) Ar annealing show that magnetic order on the Cu sublattice is present in the nonsuperconducting but removed in the superconducting samples.

Conclusions

The structural variation of the T′ phase with dopant concentration and temperature can be explained in terms of the matching of bond lengths in the copper and rare-earth coordination environments producing a tolerance factor close to 1 with no consequent requirement for structural distortion on cooling. Cerium is introduced in the +IV valence state, as shown by the increased Cu–O bond lengths and reduced c/a ratios and cell volumes. Antiferromagnetic order is the common feature of all the parent materials of the high-T_c compounds, in contrast to the variation of subtle structural features such as the buckling of the CuO_2 layers in orthorhombic as opposed to tetragonal symmetry. However, the dependence of the magnetic order on doping shows important differences between the electron- and hole-doped series. Magnetic neutron diffraction has revealed that antiferromagnetic order on the Cu sublattice is much more robust to electron doping in the T′ system than to hole doping in the K_2NiF_4-type phases. This is qualitatively explained in terms of the contrast between dilution due to nonmagnetic Cu(I) states and frustration due to holes on either the oxygen or copper sublattices. The change in the ordered moment on doping is used to estimate the average radius of a carrier which compares with that in the hole-doped O phases derived from an analysis of the localization lengths.[17] Analysis of the competition between electron kinetic energy and antiferromagnetism produces an estimate of $t = 0.8$ eV for motion

(44) Birgeneau, R. J.; Kastner, M. A.; Aharony, A. *Z. Phys. B* **1987**, *68*, 427.
(45) Lyons, K. B.; Fleury, P. A.; Remeika, J. P.; Cooper, A. S.; Negran, T. J. *Phys. Rev. B* **1988**, *37*, 2393.
(46) Mattheiss, L. F. *Phys. Rev. Lett.* **1987**, *58*, 1028.
(47) Goodenough, J. B.; Manthiram, A. *Physica C* **1989**, *157*, 439.
(48) Chen, C. H.; Werder, D. J.; James, A. C. W. P.; Murphy, D. W.; Zahurak, S. M.; Fleming, R. M.; Batlogg, B.; Schneemeyer, L. F. *Physica C* **1989**, *160*, 375.
(49) Hidaka, Y.; Suzuki, M. *Nature* **1989**, *338*, 635.
(50) Luke, G. M.; Le, L. P.; Sternlieb, B. J.; Uemura, Y. J.; Brewer, J. H.; Kadono, R.; Kiefl, R. F.; Kreitzmann, S. R.; Riseman, T. M.; Maple, M. B.; Seaman, C. L.; Kakurai, K.; Uchida, S.; Takagi, H.; Tokura, Y.; Hidaka, Y.; Murakami, T.; Gopalakrishnan, J.; Sleight, A. W.; Subramanian, M. A. *Physica C* **1989**, *162–164*, 825.

of the electron in the upper Hubbard subband. Symmetry analysis of the magnetic structure reveals the possible importance of coupling between the Nd and Cu sublattices, which is reflected in the spin direction of Nd^{3+}, the high Néel temperature (2 K), and a polarization-induced moment above T_N. A simple isotropic exchange model for the magnetic structure at high temperatures with explicit consideration of the coupling between the neodymium and copper sublattices constrains the relative values of the various exchange constants and further amplifies the importance of the interaction between the Nd and Cu sites along the *c* axis in coupling the two sublattices at the experimentally observed wavevector. This simple model also demonstrates that isotropic exchange interactions are not responsible for the observed spin reorientation transitions at high temperatures.

Acknowledgment. We thank the SERC for financial support of this work and the Institut Laue Langevin and the Rutherford Appleton Laboratory for provision of neutron time. We thank J. K. Cockcroft, A. W. Hewat, and J.-L. Soubeyroux for experimental assistance at ILL, R. M. Ibberson at RAL, and J. M. F. Gunn (RAL), D. W. Murphy, and A. C. W. P. James (AT&T Bell Laboratories) for useful discussions. M.J.R. is a Junior Research Fellow at Merton College, Oxford, England.

Supplementary Material Available: Data for the TGA determination of oxygen concentration in $Nd_{2-x}Ce_xCuO_{4-\delta}$ (Table I), final parameters derived from the Rietveld refinement of $Nd_{1.85}Ce_{0.15}CuO_{4-\delta}$ at 4.2 K (Table II), and exchange interactions involving the Cu(0,0,0) and the Nd(0,0,*z*) and Nd(0,0,$\bar{z}$) sublattices (Table V) (3 pages). Ordering information is given on any current masthead page.

Contribution from the Department of Chemistry and Biochemistry, Queens College-CUNY, Flushing, New York 11367

Effects of Ligand Planarity and Peripheral Charge on Intercalative Binding of Ru(2,2′-bipyridine)$_2$L^{2+} to Calf Thymus DNA

Robert J. Morgan, Sanjoy Chatterjee, A. David Baker,* and Thomas C. Strekas*

Received November 2, 1990

The binding of mixed-ligand complexes of the type Ru(bpy)$_2$L^{2+} (bpy = 2,2′-bipyridine and L = aromatic diimine) to calf thymus DNA has been investigated by absorption, emission, and circular dichroism spectroscopy and equilibrium dialysis binding studies. Resolved spectral features of the ligand L simplify interpretation of the spectra regarding intercalation. When L is 4′,7′-phenanthrolino-5′,6′:2,3-pyrazine (ppz), evidence of intercalative binding is provided by hypochromicity in the visible MLCT band associated with the ppz ligand as well as greatly increased emission. CD spectra of dialyzates indicate enantioselectivity associated with binding. Binding constants are comparable to those measured for Ru(phen)$_3^{2+}$ under similar conditions. For the structurally related ligand 2,3-di-2-pyridylpyrazine (dpp), which is incapable of assuming a completely planar conformation, no evidence of intercalative binding is observed. Overall binding constants for the dpp complex are too low to measure. When a metal site (-PtX$_2$) is incorporated into the complexed ppz, intercalative binding is still evident with no significant change in binding constant, but an increase in the site size (*l* parameter of the McGhee and von Hippel equation) was required to fit the data. We interpret this as due to increased disruption of the double-stranded DNA structure upon intercalation of the ppz ligand with the coordinated platinum. For a series of complexes when L is quaterpyridyl (qpy), or its mono- or dimethyl quaternary form, all complexes show evidence of binding strongly to DNA. The binding constants show the following ordering: Me$_2$qpy^{2+} > qpy ~ Meqpy$^+$. Circular dichrosim spectra of DNA dialyzates indicate that only the Me$_2$qpy^{2+} complex binds enantioselectively. Hypochromicity is observed for the visible MLCT bands of only the qpy complex, and a hyperchromic effect, accompanied by a red shift, is observed for the Me$_2$qpy^{2+} complex. This complex is also the only member of the series to show increased fluorescence (also accompanied by a red shift) in the presence of DNA. All of the data suggest a distinctly unique mode of binding for the Me$_2$qpy^{2+} complex, possibly induced by electrostatic interaction of the charged quaternary methyl groups with a pair of DNA phosphates on either chain of the double-stranded structure.

Introduction

A number of recent studies,[1-14,23,24,28,29] in particular those by Barton et al.,[1-10,13,28,29] have provided evidence for specific modes of binding of selected tris chelates of transition metals with nucleic acids. One of the most intriguing cases is provided by tris chelates

(1) Barton, J. K. *Science* **1986**, *233*, 727–734.
(2) Pyle, A. M.; Rehmann, J. P.; Meshoyrer, R.; Kumar, C. V.; Turro, N. J.; Barton, J. K. *J. Am. Chem. Soc.* **1989**, *111*, 3051–3058.
(3) Barton, J. K.; Paranawithana, S. R. *Biochemistry* **1986**, *25*, 2205–2211.
(4) Barton, J. K.; Goldberg, J. M.; Kumar, C. V.; Turro, N. J. *J. Am. Chem. Soc.* **1986**, *108*, 2081–2088.
(5) Kumar, C. V.; Barton, J. K.; Turro, N. J. *J. Am. Chem. Soc.* **1985**, *107*, 5518–5523.
(6) Barton, J. K.; Raphael, A. L. *Proc. Natl. Acad. Sci. U.S.A.* **1985**, *82*, 6460–6464.
(7) Barton, J. K.; Lolis, E. *J. Am. Chem. Soc.* **1985**, *107*, 708–709.
(8) Barton, J. K.; Basile, L. A.; Danishefsky, A.; Axexandrescu, A. *Proc. Natl. Acad. Sci. U.S.A.* **1984**, *81*, 1961–1965.
(9) Barton, J. K.; Danishefsky, A.; Goldberg, J. M. *J. Am. Chem. Soc.* **1984**, *106*, 2172–2176.
(10) Barton, J. K.; Dannenberg, J. J.; Raphael, A. L. *J. Am. Chem. Soc.* **1982**, *104*, 4967–4968.
(11) Norden, B.; Tjernfeld, F. *FEBS Lett.* **1976**, *67*, 368–370.
(12) Hiort, C.; Norden, B.; Rodger, R. *J. Am. Chem. Soc.* **1990**, *112*, 1971–1982.
(13) Goldstein, B. M.; Barton, J. K.; Berman, H. M. *Inorg. Chem.* **1986**, *25*, 842–847.
(14) Baker, A. D.; Morgan, R. J.; Strekas, T. C. *J. Am. Chem. Soc.* **1991**, *113*, 1411–1412.
(15) Hosek, W.; Tysoe, S. A.; Gafney, H. D.; Baker, A. D.; Strekas, T. C. *Inorg. Chem.* **1989**, *28*, 1228–1231.
(16) Fuchs, Y.; Lofters, S.; Dieter, T.; Shi, W.; Morgan, R.; Strekas, T. C.; Gafney, H. D.; Baker, A. D. *J. Am. Chem. Soc.* **1987**, *109*, 2691–2697.
(17) Braunstein, C. H.; Baker, A. D.; Strekas, T. C.; Gafney, H. D. *Inorg. Chem.* **1984**, *23*, 857–864.
(18) Knors, C.; Gafney, H. D.; Baker, A. D.; Braunstein, C.; Strekas, T. C. *J. Raman Spectrosc.* **1983**, *14*, 32–36.
(19) Morgan, R.; Baker, A. D. *J. Org. Chem.* **1990**, *55*, 1986–1993.
(20) Bierig, K.; Morgan, R. J.; Tysoe, S.; Gafney, H. D.; Strekas, T. C.; Baker, A. D. Submitted for publication.
(21) Baker, A. D.; Morgan, R. J.; Gafney, H. D.; Strekas, T. C. Submitted for publication.
(22) Lippard, S. J. *Science* **1982**, *218*, 1075–1082.
(23) McGhee, J. D.; von Hippel, P. H. *J. Mol. Biol.* **1974**, *86*, 469.
(24) Kelly, J. M.; Tossi, A. B.; McConnell, D. J.; OhUigin, C. *Nucleic Acids Res.* **1985**, *13*, 6017–6034.
(25) Tossi, A. B.; Kelly, J. M. *Photochem. Photobiol.* **1989**, *5*, 545–556.
(26) Wang, A. H. J.; Nathans, J.; van der Marel, G.; van Boom, J. H.; Rich, A. *Nature* **1978**, *276*, 471–474.
(27) Copper, J. B.; MacQueen, D. B.; Petersen, J. D.; Wertz, D. W. *Inorg. Chem.* **1990**, *29*, 3701–3705.
(28) Long, E. C.; Barton, J. K. *Acc. Chem. Res.* **1990**, *23*, 271–273.
(29) Rehmann, J. P.; Barton, J. K. *Biochemistry* **1990**, *29*, 1701–1709, 1710–1717.

0020-1669/91/1330-2687$02.50/0